Author Manuscript

Author Manuscript

Author Manuscript

Author Manuscript

HHS Public Access

Author manuscript

Neuron. Author manuscript; available in PMC 2020 July 17.

Published in final edited form as:

Neuron. 2019 July 17; 103(2): 235–241.e4. doi:10.1016/j.neuron.2019.05.014.

Widespread and highly correlated somato-dendritic activity in cortical layer 5 neurons

Lou Beaulieu-Laroche, **Enrique H.S. Toloza**, **Norma J. Brown**, and **Mark. T. Harnett***

Department of Brain & Cognitive Sciences and McGovern Institute for Brain Research, Massachusetts Institute of Technology, Cambridge, MA, 02139, USA.

Summary

Dendritic integration can expand the information processing capabilities of neurons. However, the recruitment of active dendritic processing in vivo and its relationship to somatic activity remain poorly understood. Here, we use two-photon GCaMP6f imaging to simultaneously monitor dendritic and somatic compartments in the awake primary visual cortex. Activity in layer 5 pyramidal neuron somas and distal apical trunk dendrites shows surprisingly high functional correlation. This strong coupling persists across neural activity levels and is unchanged by visual stimuli and locomotion. Ex vivo combined somato-dendritic patch-clamp and GCaMP6f recordings indicate that dendritic signals specifically reflect local electrogenesis triggered by dendritic inputs or high-frequency bursts of somatic action potentials. In contrast to the view that dendrites are only sparsely recruited under highly specific conditions in vivo, our results provide evidence that active dendritic integration is a widespread and intrinsic feature of cortical computation.

Graphical abstract

*Corresponding author and lead contact: Harnett (harnett@mit.edu).

Author contributions

L.B.L. designed the experiments, performed and analyzed slice experiments, acquired imaging data, analyzed in vivo experiments, prepared the figures, and wrote the manuscript. E.H.S.T performed surgeries, acquired imaging data, built analysis tools, and contributed to data analysis. N.J.B. performed surgeries and acquired imaging data. M.T.H conceived of and supervised the project.

Declaration of Interests

The authors declare no competing interests.

Publisher's Disclaimer: This is a PDF file of an unedited manuscript that has been accepted for publication. As a service to our customers we are providing this early version of the manuscript. The manuscript will undergo copyediting, typesetting, and review of the resulting proof before it is published in its final citable form. Please note that during the production process errors may be discovered which could affect the content, and all legal disclaimers that apply to the journal pertain.

Author Manuscript
Author Manuscript
Author Manuscript
Author Manuscript

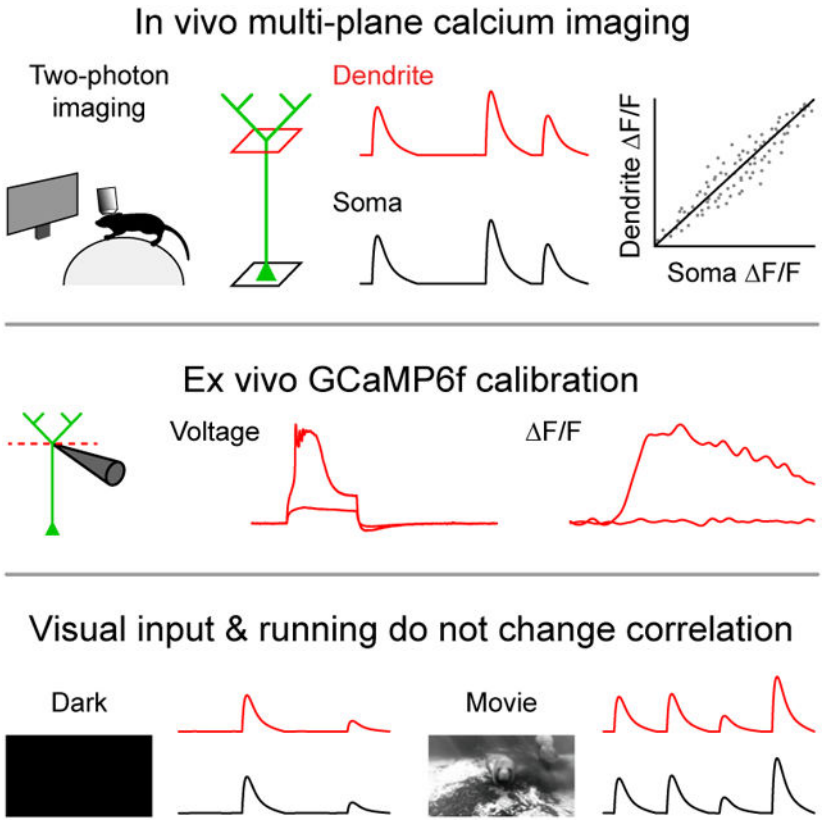

eTOC blurb

Beaulieu-Laroche et al. perform near-simultaneous calcium imaging of somatic and dendritic activity to reveal that active dendritic integration is an integral feature of information processing in cortical pyramidal neurons

Introduction

Dendrites shape how synaptic inputs are integrated into behaviorally-relevant outputs at the level of individual neurons (London and Hausser, 2005; Magee, 2000; Major et al., 2013; Stuart and Spruston, 2015). The amplification of synaptic inputs by voltage-gated ion channels can produce nonlinear dendritic spikes, which in turn trigger or modulate somatic action potential output. Layer 5 (L5) pyramidal neurons possess long apical dendrites with powerful spikes mediated by calcium electrogenesis (Harnett et al., 2013; Larkum et al., 1999; Schiller et al., 1997; Williams, 2004). Recordings in anesthetized animals demonstrated that dendritic calcium electrogenesis occurs in vivo and usually coincides with somatic burst firing (Helmchen et al., 1999). Calcium imaging has previously revealed that apical dendritic activity can represent behaviorally-relevant features in trained animals (Peters et al., 2017; Ranganathan et al., 2018; Takahashi et al., 2016; Xu et al., 2012). However, because somatic activity has not been concurrently assayed in awake animals, the relationship between compartments remains unclear. The prevalence of active dendritic integration in layer 5 is also unknown: prior experiments sparsely sampled neurons due to

Author Manuscript Author Manuscript Author Manuscript Author Manuscript

the GCaMP expression approach used and the neural dynamics during task performance. Is dendritic activity infrequent and independent of somatic activity or is it a widespread and integral aspect of cellular computation?

To determine how dendritic processing relates to cortical neuron output, we simultaneously measured dendritic and somatic GCaMP6f signals from L5 neurons in the primary visual cortex (V1) of awake mice. Because there are no existing ground truth calibrations of GCaMP6f signals in L5 somas or in dendrites, we combined multi-site whole-cell patch-clamp electrophysiology with GCaMP6f imaging in acute mouse brain slices to interpret in vivo results.

Results

We first imaged V1 neurons in awake head-fixed mice that were free to run on a cylindrical treadmill. We quasi-simultaneously recorded L5 somas (527.8 ± 9.1 μm deep, n=12 fields of view in 5 mice) and their distal apical trunk dendrites in layer 2 (167.1 ± 6.2 μm deep, 360.8 ± 6.7 μm from the soma) at 15.46 Hz using an electrically tunable lens coupled to a two-photon microscope (Figure 1A-1C). Dendritic activity was detectable in all soma-dendrite pairs that exhibited somatic transients (Figure 1E, 156/157 pairs from 5 mice). This widespread dendritic engagement was associated with synchronous activity patterns between corresponding somas and dendrites (Figure 1C & S1), resulting in dendritic and somatic signals that were strongly correlated (Figure 1D; GCaMP6f signal correlation coefficient: 0.542 ± 0.008, n=156 from 5 mice). Although corresponding somatic and dendritic GCaMP6f traces were similar, their amplitudes and kinetics were not closely matched (Figure 1C). To determine whether these differences reflect divergent features of dendritic and somatic compartments as opposed to noisy calcium dynamics or optical measurements, we analyzed soma-dendrite pairs and pairs of dendrites originating from the same soma that branched below the dendrite imaging plane (GCaMP6f signal correlation coefficient: 0.754 ± 0.033, n=29 from 5 mice). Dendritic signals consistently had faster rise and decay kinetics than somatic signals (Figure 1H-1J). Thus, corresponding somatic and dendritic GCaMP6f signals are strongly correlated but exhibit compartment-specific differences in their kinetics.

To dissect the relationship between somatic and dendritic activity, we isolated transients (Figure 2A; see methods). We found that the majority of transients were paired with a transient in the other compartment (Figure 2B; paired dendritic transient; median [Q1-Q3]: 82.3 [69.1 92.4] %; paired somatic transient; median [Q1-Q3]: 84.8 [65.8 93.3] %, n=156 from 5 mice). Furthermore, paired transients were much larger for both somas (somatic transient integral; paired, median [Q1-Q3]: 6.64 [3.69 13.32] ΔF/F*s; unpaired median [Q1-Q3]: 1.13 [0.72 1.79] ΔF/F* s; ***$p<10^{-23}$, Wilcoxon paired test, n=136 from 5 mice) and dendrites (dendritic transient integral; paired, median [Q1-Q3] 3.24 [2.42 5.06] ΔF/F*s; unpaired median [Q1-Q3]: 0.58 [0.43 0.77] ΔF/F* s; ***$p<10^{-25}$, Wilcoxon paired test, n=150 from 5 mice). To estimate how much of the activity is coupled while accounting for the different magnitudes of the paired and unpaired transients, we computed a coupling index (Figure 2D), which reflects the time integral of paired transients over the time integral of all transients. This analysis revealed that ~97% of the activity is coupled (dendrite coupling index: median [Q1-Q3]: 0.965 [0.916 0.987]; soma coupling index: median [Q1-

Author Manuscript Author Manuscript Author Manuscript Author Manuscript

Q3]: 0.972 [0.897 0.992], n=156 from 5 mice). GCaMP6f transients lasted up to minutes due to the temporal summation of multiple calcium signals. To assess coupling on a finer timescale, we separated rise and decay segments in the transients based on the first-order derivative of the GCaMP6f signal. We isolated rise events which correspond to segments with positive derivatives that likely reflect calcium entry and underlying electrical activity (Peters et al., 2017) (Figure 2E, see methods). Similar to the transients, most rise events were paired with a rise event in the other compartment (Figure 2F; paired dendritic rise event; median [Q1-Q3]: 83.9 [71.1 91.1] %; paired somatic rise event; median [Q1-Q3]: 73.4 [56.8 85.9] %, n=156 from 5 mice). Furthermore, the amplitude of rise events (maximum – minimum ΔF/F within an event) was correlated between the two compartments (Figure 2G and 2H; rise event amplitude correlation coefficient: median [Q1-Q3]: 0.554 [0.473 0.645], n=156 from 5 mice). This strong somato-dendritic coupling resulted in similar tuning between the two compartments (Figure S1). These analyses reveal that most GCaMP6f events occur concurrently in corresponding dendritic and somatic compartments.

To determine the physiological events that underlie the correlated somato-dendritic GCaMP6f transients we observed in vivo, we performed whole-cell recordings from GCaMP6f-expressing L5 neurons in acute brain slices from mouse V1 (Figure 3A). Dendritic whole-cell recordings (348.0 ± 12.8 μm from the soma, n=10 dendrites from 7 mice) revealed a nonlinear relationship between voltage and GCaMP6f fluorescence (Figure 3B-3D). Subthreshold depolarization produced negligible signals, while suprathreshold dendritic electrogenesis produced significant GCaMP6f signals (Figure 3B-3D). The amplitude of the GCaMP6f transients reflected the duration of the suprathreshold dendritic spike (Figure S2). Importantly, dendritic spikes of all durations produced significant ΔF/F changes (Figure S2). Backpropagating APs (bAPs) can evoke calcium influx into dendrites (Grienberger and Konnerth, 2012; Helmchen et al., 1996; Hill et al., 2013; Maravall et al., 2000; Markram et al., 1995; Ranganathan et al., 2018; Schiller et al., 1995; Spruston et al., 1995). Indeed, a critical frequency of bAPs (~100 Hz) has been shown to trigger dendritic electrogenesis (Larkum et al., 1999; Shai et al., 2015; Williams and Stuart, 2000). We therefore investigated whether somatically-evoked APs could elicit widespread somato-dendritic GCaMP6f signals. We performed dual whole-cell recordings (Figure 3F) and found that high-frequency bAPs (200 Hz), but not low-frequency bAPs (50 Hz), engaged dendritic electrogenesis to produce dendritic GCaMP6f signals (Figure 3E). Somatic GCaMP6f signals also displayed a strong frequency dependence (Figure 3E & 3H, n=21 cells from 9 mice), such that APs produced similar signals in the soma and dendrite (Figure 3I). Unlike L2/3 somas (Chen et al., 2013), L5 somas exhibited negligible signals for low-frequency or single APs (Figures S3). Thus, low-frequency bAPs do not underlie dendritic GCaMP6f signals, but high-frequency bursts can trigger dendritic electrogenesis to produce dendritic GCaMP6f signals. Conversely, directly triggering dendritic electrogenesis produced widespread signals by eliciting high-frequency somatic APs (Figure 3G & 3J). Our ex vivo calibration experiments demonstrate that dendritic GCaMP6f signals reflect active dendritic engagement in the form of calcium electrogenesis.

Somato-dendritic recordings in slices predict that both somatic and dendritic inputs can produce correlated GCaMP6f signals (Figure 3I & 3J). However, circuit influences including inhibition and neuromodulation could potentially disrupt this relationship in vivo. To

Author Manuscript Author Manuscript Author Manuscript Author Manuscript

determine whether somato-dendritic coordination is affected by state-dependent modulation of cortical circuit activity (Brombas et al., 2014; Hasenstaub et al., 2007; Niell and Stryker, 2010; Polack et al., 2013; Williams and Fletcher, 2019; Yaeger et al., 2019), we investigated the impact of visual stimuli and locomotion. We presented long natural movies as opposed to short repetitive stimuli to broadly activate neurons while limiting stimulus-driven correlations. Movie presentation significantly increased both dendritic and somatic activity (Figure 4A-4C) compared to a dark screen but did not alter somato-dendritic correlations (Figure 4D). We next analyzed periods in which animals were running versus when they were stationary (Figure 4E). Despite an increase in activity (Figure 4F & 4G), we observed no motion-driven changes in correlation coefficients (Figure 4H). The percentage of paired rise events and the slope of the relationship between paired events across compartments were also not affected by visual inputs and locomotion (Figure S4). Taken together, these results demonstrate that visual inputs and locomotion do not alter strong somato-dendritic GCaMP6f coupling despite pronounced activity level changes.

Discussion

By simultaneously imaging GCaMP6f in L5 distal apical dendrites and somas in awake animals, we reveal an unexpectedly broad engagement of active dendritic processing across the population of V1 L5 neurons as well as strong coupling between dendritic and somatic activity. Our ex vivo calibration experiments demonstrate that dendritic GCaMP6f signals specifically reflect dendritic electrogenesis. These dendritic spikes can trigger or be triggered by high-frequency action potentials, thereby altering the pattern of axo-somatic output (Beaulieu-Laroche et al., 2018; Harnett et al., 2013; Shai et al., 2015; Williams, 2005; Williams and Stuart, 1999). Strong correlations between somatic and dendritic compartments indicate that apical dendritic spikes are an essential feature of single-cell computation in awake cortical circuits as opposed to rare coincidence detection events. Furthermore, widespread and frequent dendritic calcium influx could have important implications for plasticity induction and learning (Bittner et al., 2017; Golding et al., 2002; Guerguiev et al., 2017; Kampa et al., 2006; Magee and Johnston, 1997; Remy and Spruston, 2007; Sjostrom and Hausser, 2006).

While GCaMP6f signals show robust functional correlation, somatic and dendritic compartments exhibit electrical compartmentalization, especially at the subthreshold level (Beaulieu-Laroche et al., 2018; Fletcher and Williams, 2019; Spruston, 2008; Stuart and Spruston, 1998; Stuart and Spruston, 2015; Williams, 2004; Williams and Stuart, 2002). Previous studies indicate that electrical interactions between somas and dendrites can be variable (Helmchen et al., 1999) and modulated by inhibition (Larkum et al., 1999; Silberberg and Markram, 2007; Takahashi et al., 2016) or neuromodulators (Brombas et al., 2014; Labarrera et al., 2018; Williams and Fletcher, 2019). We show here that the coordination of suprathreshold activity is constant in the face of visual stimuli, locomotion, and activity level changes, at least within the limits of GCaMP6f imaging. However, flexible somato-dendritic communication may occur on a shorter timescale or may not act along simple human-interpretable categories (e.g. running versus not running). We conclude that active dendritic integration is a widespread and integral feature of information processing in L5 pyramidal neurons.

Author Manuscript Author Manuscript Author Manuscript Author Manuscript

STAR Methods

CONTACT FOR REAGENT AND RESOURCE SHARING

Further information and requests for resources and reagents should be directed to and will be fulfilled by the Lead Contact, Mark T. Harnett (harnett@mit.edu).

EXPERIMENTAL MODEL AND SUBJECT DETAILS

C57BL/6 or Rbp4-Cre$^{+/-}$ mice were used for all experiments in accordance with NIH and the Massachusetts Institute of Technology Committee on Animal Care guidelines. Male mice were housed in groups (up to four) or singly before surgery and singly after surgery. Animals were maintained on a 12-hour light/dark cycle in a temperature- and humidity-controlled room with food and water *ad libitum* and used for experimentation at 7-24 weeks of age.

METHODS DETAILS

Surgery—Mice were anesthetized with isoflurane and secured in a stereotaxic apparatus. A heating pad was used to maintain body temperature; additional heating was provided until fully recovered. The scalp was shaved, wiped with hair-removal cream, and cleaned with iodine solution and ethanol. After intraperitoneal injection of Dexamethasone (4 mg/kg) and Carprofen (5mg/kg), and subcutaneous injection of slow-release Buprenorphine (0.5 mg/kg), the skull was exposed.

For in vivo imaging, using Rbp4-Cre$^{+/-}$ mice aged 8-15 weeks, a 3 mm craniotomy was drilled centered at −3.8 mm anterior-posterior, +3.0 mm lateral from bregma. 50-100 nL of AAV1-syn-flex-GCaMP6f-WPRE-SV40 were injected in 3-4 sites, 650-700 μm from the surface of the brain. Cranial windows consisting of two stacked 3 mm coverslips (~0.1 mm) under a 5 mm coverslip were inserted into the craniotomy, and the edges of the larger glass were sealed with cyanoacrylate glue and dental cement. A head-post was implanted to allow head fixation. Imaging was performed 4-12 weeks post-surgery.

For slice experiments, using mice aged 7-12 weeks, 1-3 small craniotomies (burr holes) were performed in each hemisphere centered at −3.8 mm anterior-posterior, ±3.0 mm lateral from bregma. 50-100 nL of the GCaMP6f virus described above were injected at each site at 650-750 μm from the surface of the brain in Rpb4-Cre+/− mice. For C57BL/6 wild-type, the GCaMP6f virus was mixed in equal part with a diluted AAV1-syn-Cre virus at 650-750 μm or 150 μm (for L2/3; Figure S3) from the surface of the brain. Injected animals, including those some of those used for in vivo imaging, were used for slice physiology 4-12 weeks post-surgery.

Two-photon imaging—Imaging from behaving animals was performed with a Neurolabware standard microscope (http://neurolabware.com/microscope) equipped with GaAsP photomultiplier tubes. GCaMP6f was excited with a 980 nm ultrafast pulsed laser beam from a dispersion-compensated Insight DeepSee coupled to a 4x passive pulse splitter to reduce photodamage and bleaching (Ji et al., 2008). A water immersion objective (Nikon 16×, 0.8 NA) was used for excitation and emission collection. Bi-directional frames

Author Manuscript Author Manuscript Author Manuscript Author Manuscript

(512×796 pixels) were simultaneously acquired at two planes with an electrically-tunable lens (Optotune EL-10-30-NIR-LD) at 30.92 Hz (15.46 Hz for each plane). Z-stacks (1000-1500 frames every 5-7 μm) were acquired at the end of the experiments. Laser beam intensity was independently controlled with electro-optical modulators.

Visual stimuli were presented on the contralateral side via a monitor 20 cm from the mouse's eye. Stimuli were luminance-normalized and spherically warped to compensate for the wide-angle field-of-view of the mice (http://help.brain-map.org/display/observatory/Documentation). A dark, opaque plastic cylinder was attached to the head-plate and surrounded the objective to limit light contamination from the monitor. Before imaging, animals were acclimatized over the course of several days to head-fixation on the behavior rig equipped with a cylindrical treadmill. For experiments in Figures 1, 2, 4, S1A and S4, mice were presented with natural movies (black-and-white clips lasting 20-30 seconds). They were repeated ten times in a random order, separated by a ten-second gray screen. A black screen was presented before and after the visual stimuli series for 10-20 minutes each time. For experiments in Figure S1B-S1G, we presented only drifting gratings in separate imaging sessions. Drifting gratings (square waveform) were displayed for two seconds, followed by a five-second gray screen. Ten repetitions of each grating type were presented in a random order each session, sampled from eight orientations (0 to 315° in 45° increments) and four temporal frequencies (1, 2, 4, and 8 Hz), with a spatial frequency of 0.05 cycles/degree.

An in vitro galvanometer-based multiphoton microscope system (Bruker Ultima) with a water-immersion lens (60×, 0.9 NA) was used to image brain slices. A dispersion-compensated Mai-Tai DeepSee laser was used to excite Alexa 594 at 880 nm and GCaMP6f at 920 nm (separated via dichroic mirrors to independent sets of GaAsP photosensor modules). Another photosensor module was used to collect transmitted-light Dodt gradient images for patch-clamp targeting. Laser beam intensity was independently controlled with electro-optical modulators. Line scan imaging was performed at somatic and dendritic sites at 400-1000 Hz with dwell times of 8 μs. Line scan and frame scan imaging produced comparable signals (Figure S3).

Cortical slice preparation—Cortical brain slices were prepared from adult (>11 weeks old) mice using methods previously described (Beaulieu-Laroche and Harnett, 2018; Beaulieu-Laroche et al., 2018). Mice were deeply anesthetized with isoflurane in balanced oxygen prior to immediate decapitation. 300 μm slices were prepared from the visual cortex. Slicing was performed with a vibrating blade microtome in ice-cold slicing artificial cerebrospinal fluid (aCSF) containing (in mM): sucrose 160, sodium bicarbonate 28, potassium chloride 2.5, sodium phosphate monobasic monohydrate 1.25, calcium chloride 1, magnesium chloride 7.5, glucose 7.25, HEPES 20, sodium pyruvate 3, and sodium ascorbate 3, 295-305 mOsm, saturated with 95% O_2 and 5% CO_2. Slices were then incubated for ~30 minutes at 35.5 °C in recovery aCSF containing (in mM): sodium chloride 92, sodium bicarbonate 28.5, potassium chloride 2.5, sodium phosphate monobasic monohydrate 1.2, calcium chloride 2, magnesium chloride 4, glucose 25, HEPES 20, sodium pyruvate 3, and sodium ascorbate 5, 300-310 mOsm, saturated with 95% O_2 and 5% CO_2. Slices were kept in recovery aCSF at 18 °C until use.

Author Manuscript Author Manuscript Author Manuscript Author Manuscript

Patch-clamp recording—Patch-clamp recordings were performed from the soma and apical dendrites of pyramidal neurons at 34-36 °C in recording aCSF containing (in mM): sodium chloride 120, potassium chloride 3, sodium bicarbonate 25, sodium phosphate monobasic monohydrate 1.25, calcium chloride 1.2, magnesium chloride 1.2, glucose 11, sodium pyruvate 3, and sodium ascorbate 1, 300-305 mOsm, saturated with 95% O_2 and 5% CO_2. Except for Figure S3G and S3H, recordings were restricted to GCaMP6f+ neurons with cytosolic baseline fluorescence and nuclear exclusion. Whole-cell dialysis did not impact GCaMP6f signals (Figure S3). Current-clamp recordings were performed in bridge mode with an Axopatch 200B or a Dagan BVC-700A amplifier with bridge fully balanced. Patch pipettes were made from thick-wall glass (1.5 O.D., 0.75 I.D.) or thin-wall glass (1.5 O.D., 1.1 I.D.). Pipettes had resistances ranging from 5 to 15 MΩ, and capacitance was fully neutralized prior to break-in. Series resistances ranged from 10-30 MΩ. The intracellular solution contained (in mM): potassium gluconate 134, potassium chloride 6, HEPES 10, sodium chloride 4, adenosine 5′-triphosphate magnesium 4, guanosine 5′-triphosphate sodium 3, phosphocreatine di (tris) 14, and Alexa 594 0.05. For experiments in Figure S3G and S3H, 0.1 mM Oregon Bapta Green-1 (OGB-1) was added to the internal solution. Liquid junction potential was not corrected for. Current and voltage signals were filtered at 10 kHz and acquired at 20 kHz.

To elicit somatic action potentials, step current injection (2 ms) of constant amplitudes (1-3 nA) were employed. Dendritic spikes were elicited through suprathreshold step current injections of constant amplitude (300-1000 pA) for various durations (Figure S2).

QUANTIFICATION AND STATISTICAL ANALYSIS

All analyses were performed using custom-written MATLAB codes. In vivo imaging data was rigidly motion-corrected. Regions-of-interest (ROIs) were manually drawn on all the detectable somas. With the use of Z-stacks, corresponding dendritic ROIs were then drawn. Dendritic ROIs were excluded when spatially overlapping with other dendritic segments or when the path from the soma to the dendrite intersected with other dendrites. One soma-dendrite pair showed no transients for the whole recording session (correlation coefficient = 0.02) and was excluded from the analyses. Soma-dendrite pairs from different neurons (Figure 1D) correspond to all possible combinations of unpaired somas and dendrites from the same imaging sessions. Light contamination from the monitor was subtracted following robust regression of the baselined contamination fluorescence against each ROI's raw fluorescence. To compute ΔF/F, the baseline F was estimated as the 10^{th} percentile of the fluorescence using a 160 s rolling-window. For figure display, signals were low-pass filtered at 4 Hz with zero-phase filtering using the MATLAB function filtfilt.

To detect transients, we first computed the mean and standard deviation of the raw signal without transients (<0.2 ΔF/F) and defined threshold A as 3 standard deviations above the mean and threshold B as 1 standard deviation above the mean. We then low-pass filtered (filtfilt) the raw signal at 2 Hz and identified transients as points that were above threshold A. The start and end of each transient were defined as the points in the filtered signal that crossed threshold B. Overlapping transient were combined. To compare the paired and unpaired transient integrals, only cells with both paired and unpaired transients were used.

Author Manuscript Author Manuscript Author Manuscript Author Manuscript

To detect events and decays, we computed the derivative of the filtered signal and low-pass filtered (filtfilt) it at 0.5 Hz. Rise events were identified as points in the filtered signals that were above threshold A and where the derivative was positive. The start and end of each event were defined as the points in the filtered signal that crossed threshold B or where the derivative crossed zero. Decay events were identified as points in the filtered signals that were above threshold A and where the derivative was negative. The start and end of each event were defined as the points in the filtered signal that crossed threshold B or where the derivative crossed zero. Overlapping events were combined.

For analyses in figures 1 and 2, the whole recording sessions with the movies and the dark periods were used. The recording sessions were separated as dark versus movie and stationary versus running for figures 4 and S4. Running speed was low-pass filtered (filtfilt) at 0.05 Hz, and 2.5 cm/s was used as the threshold to detect moving epochs. The percentage of paired events was computed only for pairs with events in both conditions (Figure S4C and S4E). The slope of rise events was computed only for pairs with at least 20 paired events in both conditions (Figure S4D and S4F).

For grating responses, we computed ΔF/F for each trial using the mean of the two seconds preceding the onset of the stimulus. We then averaged the ten trials for each condition and computed the mean responses during the two-second stimulus presentation. We determined whether the soma and dendrite of each pair were visually-responsive by computing a one-way ANOVA ($p<0.05$) across the 32 conditions. Using nine fields of views from three mice, we found 34 out of 66 soma-dendrite pairs with at least one visually-responsive compartment. We then averaged the somatic and dendritic tuning curves to determine the preferred temporal frequency. The tuning curves and preferred orientation of corresponding somas and dendrites were then computed at that preferred temporal frequency.

Voltage signals were low-pass filtered at 5 kHz with zero-phase filtering using the MATLAB function filtfilt for some experiments. Line scan signals were low-pass filtered at 75 Hz with zero-phase filtering using the MATLAB function filtfilt. 1-10 trials were acquired per condition and averaged for both electrophysiological and optical traces. To compute ΔF/F, the baseline F was computed using 50-100 ms of baseline signals before eliciting spikes. Morphological and distance measurements for slice experiments were performed using ImageJ/FIJI (National Institutes of Health) on two-dimensional maximal intensity projections of 1.5–2 μm Z-series collected at the end of the experiment.

Statistical analysis was performed in MATLAB. D'Agostino-Pearson tests were used to assess normality. For normal data, results are presented as mean ± SEM. For skewed data, the median and the lower and upper quartiles (Q1-Q3) are reported, and a Wilcoxon paired test or Wilcoxon rank sum test was used for statistical comparisons using MATLAB. Statistical details can be found in the figure legends and in the main text. Reported n values can be found in the figure legends and in the results. They include the number of pairs for in vivo results or recordings for ex vivo results, and the number of mice from which they were obtained.

Author Manuscript Author Manuscript Author Manuscript Author Manuscript

Supplementary Material

Refer to Web version on PubMed Central for supplementary material.

Acknowledgments

We thank Michale Fee, Sabbi Lall, Michael Tadross, Benjamin Scott, Richard Naud, and Jens Krembow for comments on the manuscript. We thank Marissa Hansen for help with illustration and for comments on the manuscript. We thank Lukas Fischer for help with the headfixed behavioral setup and members of the Harnett lab for constructive criticism on the project. We acknowledge the support of the Natural Sciences and Engineering Research Council of Canada (NSERC) [PGSD2-517068-2018] (to L.B.L). Support was provided by NIH RO1NS106031 (to M.T.H.) and NIH T32GM007753 (to E.H.S.T.). M.T.H is a Klingenstein-Simons Fellow and Vallee Foundation Scholar.

References

Beaulieu-Laroche L, and Harnett MT (2018). Dendritic Spines Prevent Synaptic Voltage Clamp. Neuron 97, 75–82.e73. [PubMed: 29249288]

Beaulieu-Laroche L, Toloza EHS, van der Goes MS, Lafourcade M, Barnagian D, Williams ZM, Eskandar EN, Frosch MP, Cash SS, and Harnett MT (2018). Enhanced Dendritic Compartmentalization in Human Cortical Neurons. Cell 175, 643–651.e614. [PubMed: 30340039]

Bittner KC, Milstein AD, Grienberger C, Romani S, and Magee JC (2017). Behavioral time scale synaptic plasticity underlies CA1 place fields. Science (New York, NY) 357, 1033–1036.

Brombas A, Fletcher LN, and Williams SR (2014). Activity-dependent modulation of layer 1 inhibitory neocortical circuits by acetylcholine. The Journal of neuroscience : the official journal of the Society for Neuroscience 34, 1932–1941. [PubMed: 24478372]

Chen TW, Wardill TJ, Sun Y, Pulver SR, Renninger SL, Baohan A, Schreiter ER, Kerr RA, Orger MB, Jayaraman V, et al. (2013). Ultrasensitive fluorescent proteins for imaging neuronal activity. Nature 499, 295–300. [PubMed: 23868258]

Fletcher LN, and Williams SR (2019). Neocortical Topology Governs the Dendritic Integrative Capacity of Layer 5 Pyramidal Neurons. Neuron 101, 76–90.e74. [PubMed: 30472076]

Golding NL, Staff NP, and Spruston N (2002). Dendritic spikes as a mechanism for cooperative long-term potentiation. Nature 418, 326–331. [PubMed: 12124625]

Grienberger C, and Konnerth A (2012). Imaging Calcium in Neurons. Neuron 73, 862–885. [PubMed: 22405199]

Guerguiev J, Lillicrap TP, and Richards BA (2017). Towards deep learning with segregated dendrites. eLife 6.

Harnett MT, Xu NL, Magee JC, and Williams SR (2013). Potassium channels control the interaction between active dendritic integration compartments in layer 5 cortical pyramidal neurons. Neuron 79, 516–529. [PubMed: 23931999]

Hasenstaub A, Sachdev RN, and McCormick DA (2007). State changes rapidly modulate cortical neuronal responsiveness. The Journal of neuroscience : the official journal of the Society for Neuroscience 27, 9607–9622. [PubMed: 17804621]

Helmchen F, Imoto K, and Sakmann B (1996). Ca2+ buffering and action potential-evoked Ca2+ signaling in dendrites of pyramidal neurons. Biophysical journal 70, 1069–1081. [PubMed: 8789126]

Helmchen F, Svoboda K, Denk W, and Tank DW (1999). In vivo dendritic calcium dynamics in deep-layer cortical pyramidal neurons. Nature neuroscience 2, 989–996. [PubMed: 10526338]

Hill DN, Varga Z, Jia H, Sakmann B, and Konnerth A (2013). Multibranch activity in basal and tuft dendrites during firing of layer 5 cortical neurons in vivo. Proceedings of the National Academy of Sciences of the United States of America 110, 13618–13623. [PubMed: 23904480]

Ji N, Magee JC, and Betzig E (2008). High-speed, low-photodamage nonlinear imaging using passive pulse splitters. Nature methods 5, 197–202. [PubMed: 18204458]

Author Manuscript Author Manuscript Author Manuscript Author Manuscript

Kampa BM, Letzkus JJ, and Stuart GJ (2006). Requirement of dendritic calcium spikes for induction of spike-timing-dependent synaptic plasticity. The Journal of physiology 574, 283–290. [PubMed: 16675489]

Labarrera C, Deitcher Y, Dudai A, Weiner B, Kaduri Amichai A, Zylbermann N, and London M (2018). Adrenergic Modulation Regulates the Dendritic Excitability of Layer 5 Pyramidal Neurons In Vivo. Cell reports 23, 1034–1044. [PubMed: 29694883]

Larkum ME, Kaiser KM, and Sakmann B (1999). Calcium electrogenesis in distal apical dendrites of layer 5 pyramidal cells at a critical frequency of back-propagating action potentials. Proceedings of the National Academy of Sciences of the United States of America 96, 14600–14604. [PubMed: 10588751]

London M, and Hausser M (2005). Dendritic computation. Annual review of neuroscience 28, 503–532.

Magee JC (2000). Dendritic integration of excitatory synaptic input. Nature reviews Neuroscience 1, 181–190. [PubMed: 11257906]

Magee JC, and Johnston D (1997). A synaptically controlled, associative signal for Hebbian plasticity in hippocampal neurons. Science (New York, NY) 275, 209–213.

Major G, Larkum ME, and Schiller J (2013). Active properties of neocortical pyramidal neuron dendrites. Annual review of neuroscience 36, 1–24.

Maravall M, Mainen ZF, Sabatini BL, and Svoboda K (2000). Estimating intracellular calcium concentrations and buffering without wavelength ratioing. Biophysical journal 78, 2655–2667. [PubMed: 10777761]

Markram H, Helm PJ, and Sakmann B (1995). Dendritic calcium transients evoked by single back-propagating action potentials in rat neocortical pyramidal neurons. The Journal of physiology 485 (Pt 1), 1–20. [PubMed: 7658365]

Niell CM, and Stryker MP (2010). Modulation of visual responses by behavioral state in mouse visual cortex. Neuron 65, 472–479. [PubMed: 20188652]

Peters AJ, Lee J, Hedrick NG, O'Neil K, and Komiyama T (2017). Reorganization of corticospinal output during motor learning. 20, 1133–1141.

Polack PO, Friedman J, and Golshani P (2013). Cellular mechanisms of brain state-dependent gain modulation in visual cortex. Nature neuroscience 16, 1331–1339. [PubMed: 23872595]

Ranganathan GN, Apostolides PF, Harnett MT, and Xu NL (2018). Active dendritic integration and mixed neocortical network representations during an adaptive sensing behavior. 21, 1583–1590.

Remy S, and Spruston N (2007). Dendritic spikes induce single-burst long-term potentiation. Proceedings of the National Academy of Sciences of the United States of America 104, 17192–17197. [PubMed: 17940015]

Schiller J, Helmchen F, and Sakmann B (1995). Spatial profile of dendritic calcium transients evoked by action potentials in rat neocortical pyramidal neurones. The Journal of physiology 487 (Pt 3), 583–600. [PubMed: 8544123]

Schiller J, Schiller Y, Stuart G, and Sakmann B (1997). Calcium action potentials restricted to distal apical dendrites of rat neocortical pyramidal neurons. The Journal of physiology 505 (Pt 3), 605–616. [PubMed: 9457639]

Shai AS, Anastassiou CA, Larkum ME, and Koch C (2015). Physiology of layer 5 pyramidal neurons in mouse primary visual cortex: coincidence detection through bursting.PLoS computational biology 11, e1004090. [PubMed: 25768881]

Silberberg G, and Markram H (2007). Disynaptic inhibition between neocortical pyramidal cells mediated by Martinotti cells. Neuron 53, 735–746. [PubMed: 17329212]

Sjostrom PJ, and Hausser M (2006). A cooperative switch determines the sign of synaptic plasticity in distal dendrites of neocortical pyramidal neurons. Neuron 51, 227–238. [PubMed: 16846857]

Spruston N (2008). Pyramidal neurons: dendritic structure and synaptic integration. Nature reviews Neuroscience 9, 206–221. [PubMed: 18270515]

Spruston N, Schiller Y, Stuart G, and Sakmann B (1995). Activity-dependent action potential invasion and calcium influx into hippocampal CA1 dendrites. Science (New York, NY) 268, 297–300.

Author Manuscript Author Manuscript Author Manuscript Author Manuscript

Stuart G, and Spruston N (1998). Determinants of voltage attenuation in neocortical pyramidal neuron dendrites. The Journal of neuroscience : the official journal of the Society for Neuroscience 18, 3501–3510. [PubMed: 9570781]

Stuart GJ, and Spruston N (2015). Dendritic integration: 60 years of progress. Nature neuroscience 18, 1713–1721. [PubMed: 26605882]

Takahashi N, Oertner TG, Hegemann P, and Larkum ME (2016). Active cortical dendrites modulate perception. Science (New York, NY) 354, 1587–1590.

Williams SR (2004). Spatial compartmentalization and functional impact of conductance in pyramidal neurons. Nature neuroscience 7, 961–967. [PubMed: 15322550]

Williams SR (2005). Encoding and decoding of dendritic excitation during active states in pyramidal neurons. The Journal of neuroscience : the official journal of the Society for Neuroscience 25, 5894–5902. [PubMed: 15976078]

Williams SR, and Fletcher LN (2019). A Dendritic Substrate for the Cholinergic Control of Neocortical Output Neurons. Neuron 101, 486–499.e484. [PubMed: 30594427]

Williams SR, and Stuart GJ (1999). Mechanisms and consequences of action potential burst firing in rat neocortical pyramidal neurons. The Journal of physiology 521 Pt 2, 467–482. [PubMed: 10581316]

Williams SR, and Stuart GJ (2000). Backpropagation of physiological spike trains in neocortical pyramidal neurons: implications for temporal coding in dendrites. The Journal of neuroscience : the official journal of the Society for Neuroscience 20, 8238–8246. [PubMed: 11069929]

Williams SR, and Stuart GJ (2002). Dependence of EPSP efficacy on synapse location in neocortical pyramidal neurons. Science (New York, NY) 295, 1907–1910.

Xu NL, Harnett MT, Williams SR, Huber D, O'Connor DH, Svoboda K, and Magee JC (2012). Nonlinear dendritic integration of sensory and motor input during an active sensing task. Nature 492, 247–251. [PubMed: 23143335]

Yaeger CE, Ringach DL, and Trachtenberg JT (2019). Neuromodulatory control of localized dendritic spiking in critical period cortex. Nature.

Author Manuscript Author Manuscript Author Manuscript Author Manuscript

Highlights

- Layer 5 neuron apical dendrites exhibit frequent GCaMP6f signals
- Calcium electrogenesis underlies dendritic GCaMP6f signals
- Dendritic activity is highly correlated with somatic activity
- Visual stimuli and running do not change somato-dendritic GCaMP6f correlation

Author Manuscript Author Manuscript Author Manuscript Author Manuscript

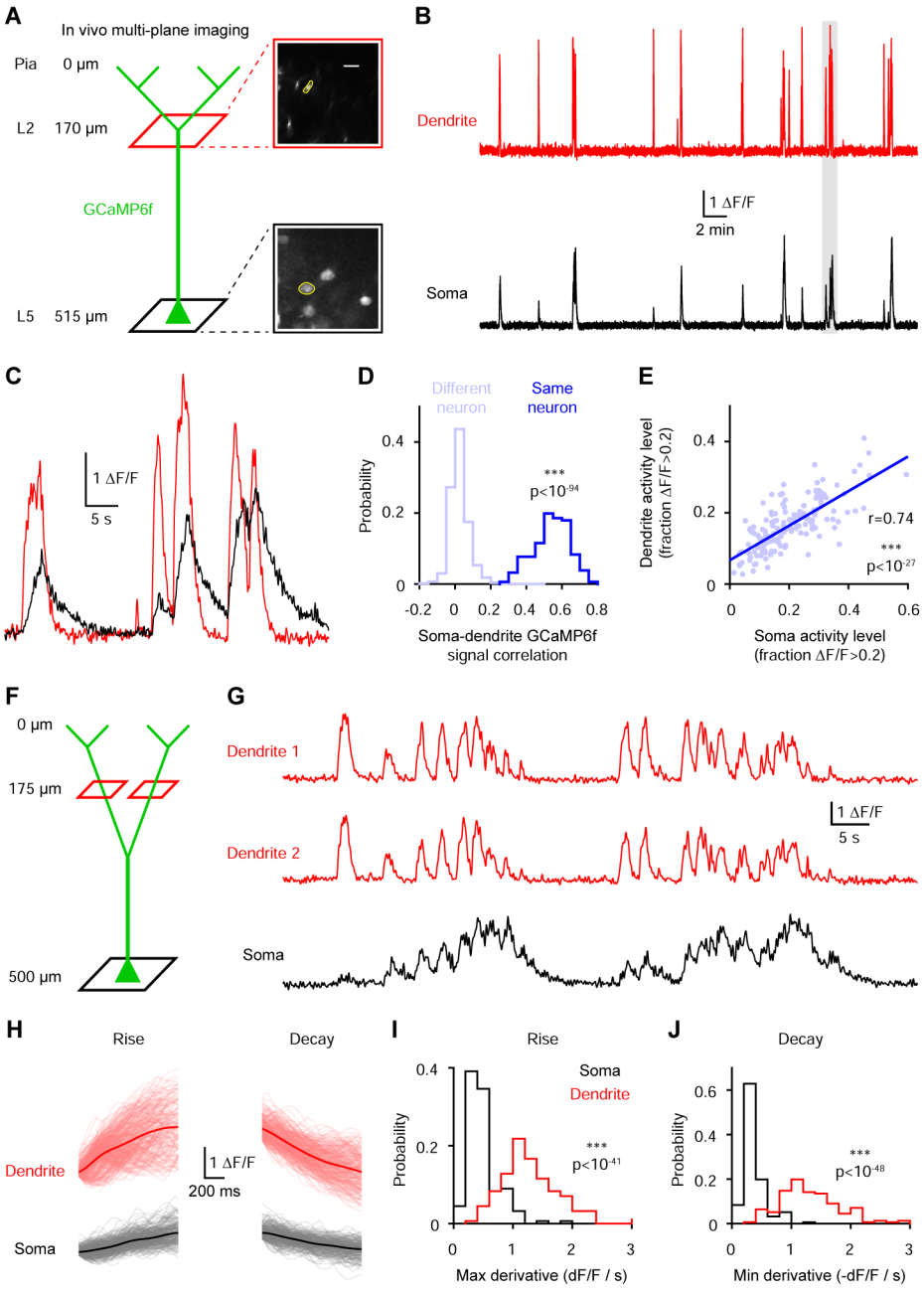

Figure 1. Dendritic GCaMP6f signals are widespread across the population and highly correlated with somatic signals.

(A) Left, experimental approach to simultaneously record somatic and dendritic signals from L5 pyramidal neurons. Right, two-photon mean image at the two imaging planes. The yellow regions highlight a soma and its corresponding dendrite.

(B) Near-simultaneously recorded two-photon GCaMP6f traces from the soma and dendrite shown in A.

(C) Expanded traces from B corresponding to the segment with the gray dashed box.

(D) GCaMP6f signal correlation coefficients for soma-dendrite pairs from the same (n=156 pairs) or different (n=1702) neurons (***$p<10^{-94}$, Wilcoxon rank sum test) from 5 mice.

Author Manuscript Author Manuscript Author Manuscript Author Manuscript

(E) Relationship between somatic and dendritic activity levels across soma-dendrite pairs (correlation: r=0.74, ***$p<10^{-27}$, n=156 pairs from 5 mice).
(F) Experimental approach to record pairs of dendrites from the same soma.
(G) Simultaneously recorded two-photon GCaMP6f traces from the soma and the two dendrites illustrated in F.
(H) Rise and decay events (see methods) for the soma and dendrite 1 in G. Gray and light red lines represent individual events (up to 1 s) while averages are shown in black and red.
(I) Average maximal derivative for all rise events of each dendrite and soma (***$p<10^{-41}$, Wilcoxon rank sum test, n=156 pairs from 5 mice).
(J) Average minimal derivative for all decay events of each dendrite and soma (***$p<10^{-48}$, Wilcoxon rank sum test, n=156 pairs from 5 mice).
See also Figure S1.

Author Manuscript Author Manuscript Author Manuscript Author Manuscript

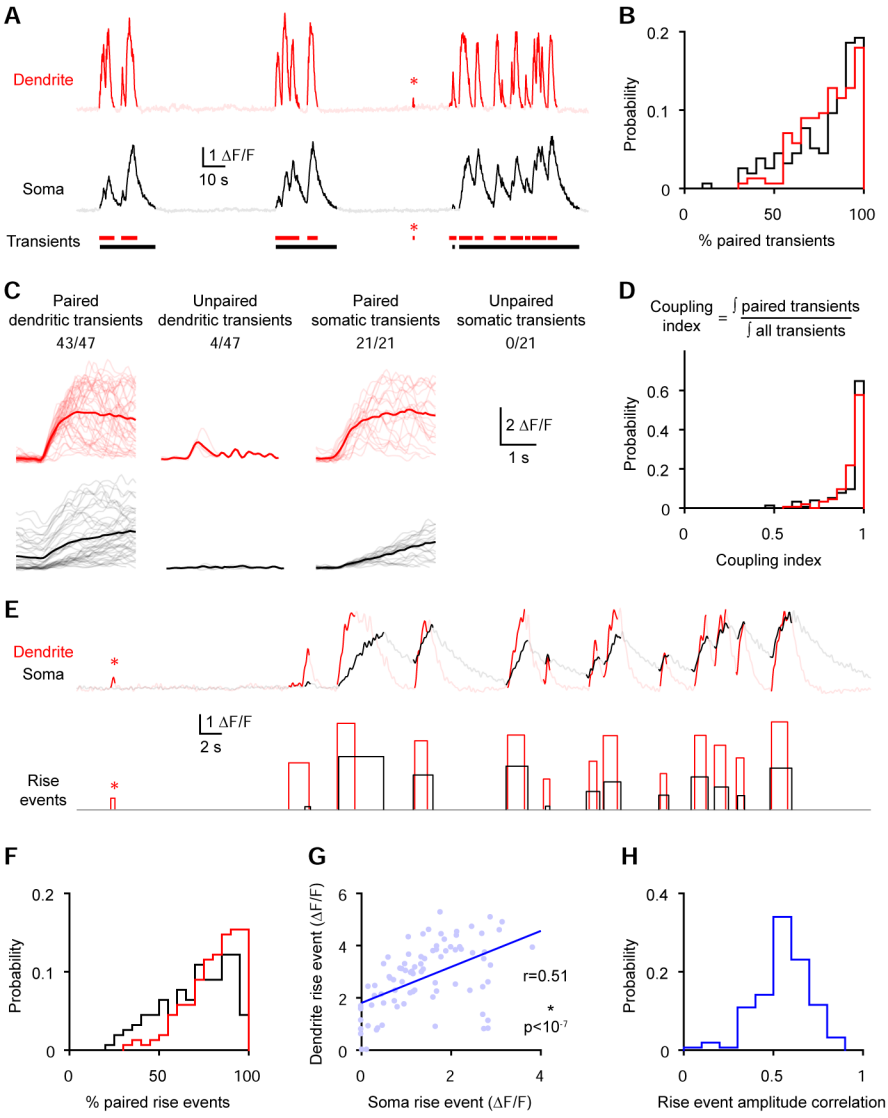

Figure 2. The majority of GCaMP6f transients are paired between corresponding somas and dendrites.

(A-C) Somatic and dendritic transients were categorized as paired or unpaired based on their temporal overlap with transients in the other compartment.

(A) GCaMP6f signals from the soma and dendrite with detected transients shown in solid colors. The asterisk highlights an unpaired dendritic transient.

(B) Percentage of paired somatic and dendritic events (n=156 pairs from 5 mice).

(C) Events from the neuron shown in A categorized as paired and unpaired. Gray and light red lines represent individual transients (750 ms before the onset and up to 2600 ms after) while averages are shown in black and red. The number of paired or unpaired transients over the total number of transients is indicated above each panel.

(D) Coupling index for all soma-dendrite pairs (n=156 pairs from 5 mice).

(E-H) Rise events (segments of transients with positive derivative) were categorized as paired or unpaired based on their overlap with rise events in the other compartment.

Author Manuscript Author Manuscript Author Manuscript Author Manuscript

(E) GCaMP6f signals from the soma and dendrite with detected rise events shown in solid colors. The asterisk highlights an unpaired dendritic rise event.
(F) Percentage of paired dendritic and somatic rise events (n=156 pairs from 5 mice).
(G) Relationship between the amplitude of dendritic and somatic rise events of the neuron shown in E (correlation: r=0.51, ***$p<10^{-7}$, n=85 rise events).
(H) Correlation coefficients for rise event amplitudes for soma-dendrite pairs (n=156 pairs from 5 mice).

Author Manuscript Author Manuscript Author Manuscript Author Manuscript

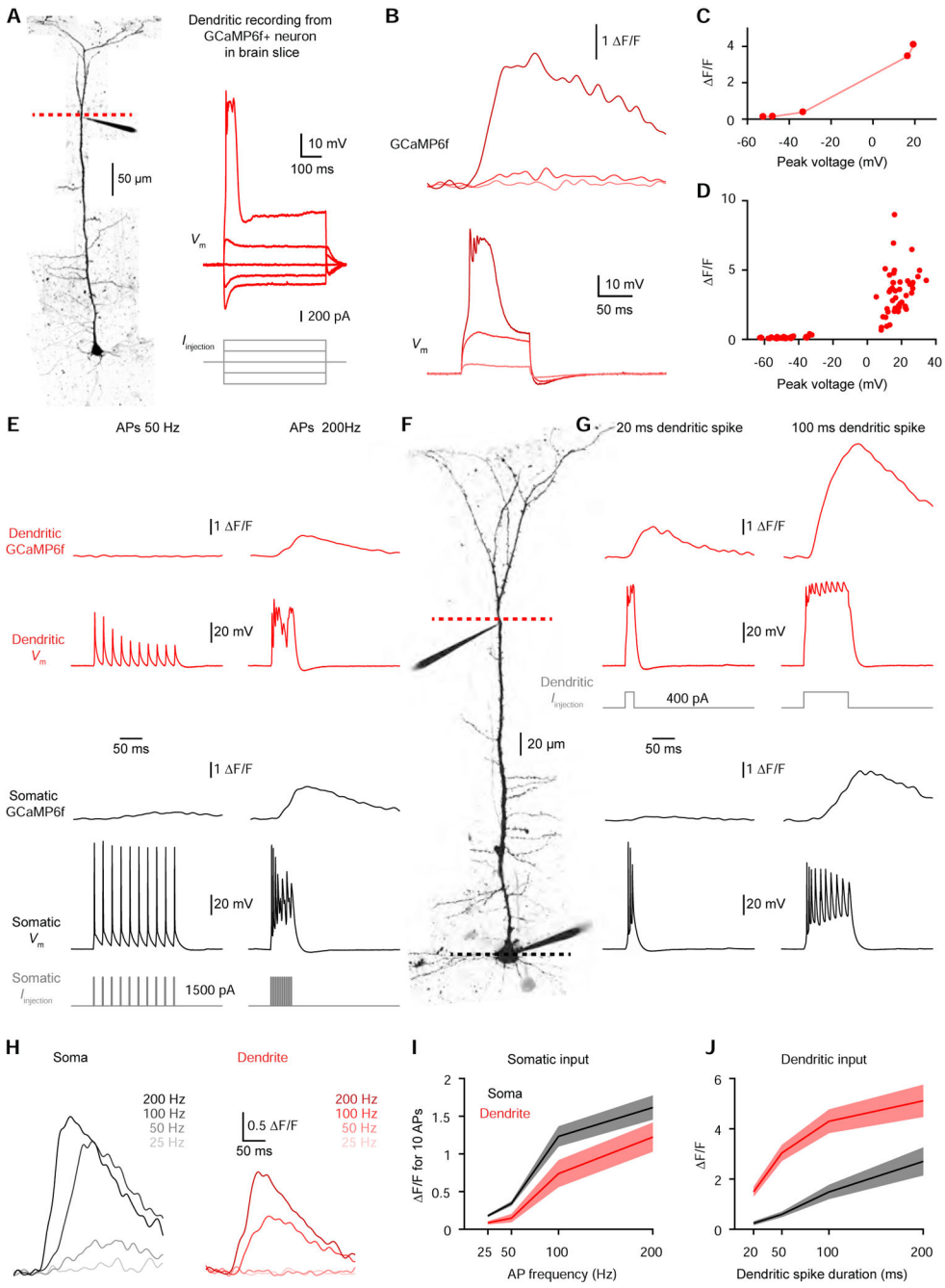

Figure 3. Ex vivo calibration of dendritic GCaMP6f signals.

(A) Left, two-photon Z-stack montage image of a GCaMP6f-expressing mouse L5 neuron. The dashed line indicates the location for calcium imaging next to the dendritic patch clamp electrode 373 µm from the soma. Right, dendritic voltage (top) in response to step current injection (bottom).

(B) Dendritic GCaMP6f signal (top) associated with dendritic voltage (bottom).

(C) GCaMP6f peak as a function of peak voltage for increasing 100 ms step current injections for the dendrite shown in A-C.

Author Manuscript Author Manuscript Author Manuscript Author Manuscript

(D) Dendritic GCaMP6f peak as a function of peak voltage for increasing 100 ms step current injections (n=10 dendrites from 7 mice).
(E) Membrane potential and GCaMP6f signals at the dendrite (red; top) and soma (black; bottom) during slow (50 Hz; left) and fast (200 Hz; right) APs evoked by somatic current injection (gray) in the neuron shown in F.
(F) Two-photon image of a GCaMP6f-expressing L5 neuron with somatic and dendritic (320 μm from the soma) patch clamp electrodes.
(G) Membrane potential and GCaMP6f signals at the dendrite (red; top) and soma (black; bottom) during short (20 ms; left) and long (100 ms; right) dendritic spikes evoked by dendritic current injection (light red) in the neuron shown in F.
(H) GCaMP6f signals at the soma (left) and dendrite (right) for 10 somatic APs at the indicated frequencies in the neuron shown in F.
(I) Somatic (black) and dendritic (red) GCaMP6f peak for 10 APs as a function of AP frequency (n=21 neurons from 9 mice). Pooled data represent mean ± SEM.
(J) Somatic (black) and dendritic (red) GCaMP6f peak as a function of dendritic spike duration (n=10 neurons from 7 mice). Pooled data represent mean ± SEM.
See also Figures S2 and S3.

Author Manuscript Author Manuscript Author Manuscript Author Manuscript

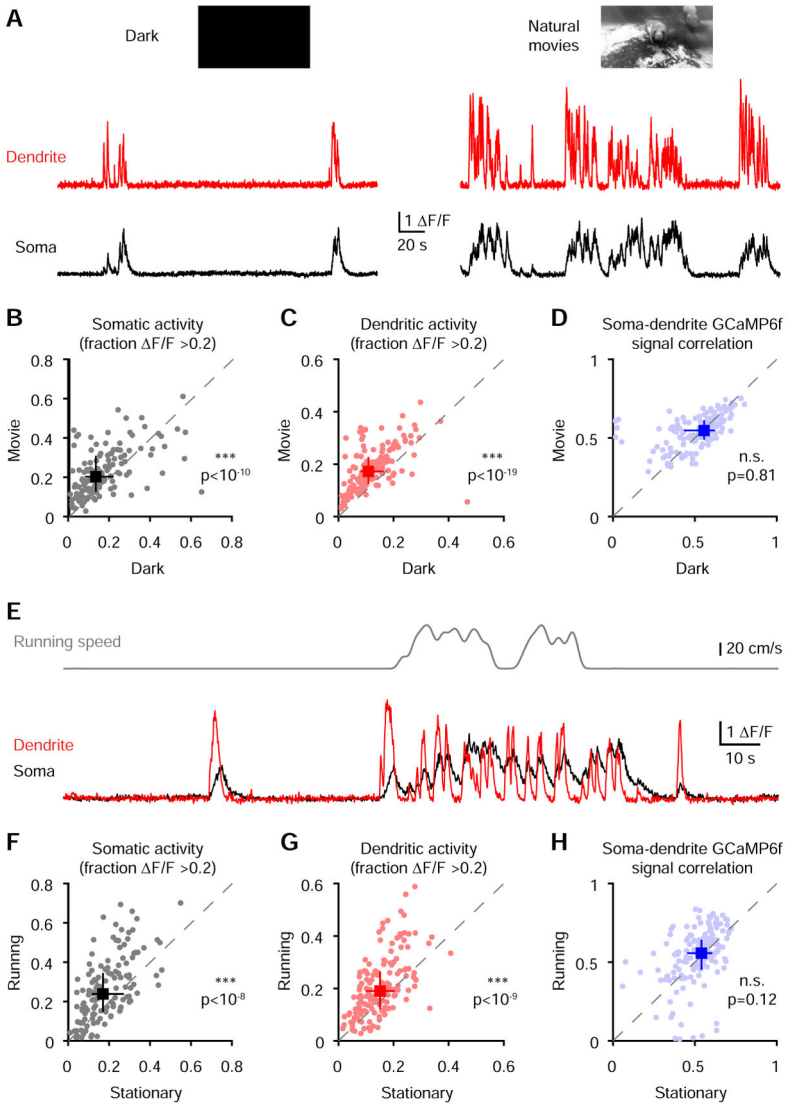

Figure 4. Somato-dendritic GCaMP6f correlations are conserved across activity levels and unchanged by visual stimuli and locomotion.

(A) GCaMP6f signals from a soma and its corresponding dendrite during dark screen (left) or the presentation of natural movies (right).

(B) Comparison of somatic activity level (***$p<10^{-10}$, Wilcoxon paired test, n=156 pairs from 5 mice) during the dark and natural movie epochs.

(C) Comparison of dendritic activity level (***$p<10^{-19}$, Wilcoxon paired test, n=156 pairs from 5 mice) during the dark and natural movie epochs.

(D) Comparison of correlation coefficients (p=0.81, Wilcoxon paired test, n=156 pairs from 5 mice) in soma-dendrite pairs during the dark and natural movie epochs. The leftward point cluster represents neurons that were silent in the dark.

(E) GCaMP6f signals from the soma and dendrite (bottom) with running speed trace (top).

(F) Comparison of somatic activity level (***$p<10^{-8}$, Wilcoxon paired test, n=156 pairs from 5 mice) during the stationary and running epochs.

Author Manuscript Author Manuscript Author Manuscript Author Manuscript

(G) Comparison of dendritic activity level (***$p<10^{-9}$, Wilcoxon paired test, n=156 pairs from 5 mice) during the stationary and running epochs.
(H) Comparison of correlation (p=0.12, Wilcoxon paired test, n=156 pairs from 5 mice) in paired soma-dendrite during the stationary and running epochs.
Pooled data represent median and interquartile range for B-D and F-H.
See also Figure S4.

Author Manuscript Author Manuscript Author Manuscript Author Manuscript

KEY RESOURCES TABLE

REAGENT or RESOURCE	SOURCE	IDENTIFIER
Bacterial and Virus Strains		
AAV1-syn-flex-GCaMP6f-WPRE-SV40	Addgene/Penn Vectors	Cat#: 100833-AAV1
Chemicals, Peptides, and Recombinant Proteins		
Adenosine 5′-triphosphate magnesium salt	Sigma	Cat#: A9187; CAS: 74804-12-9
Alexa Fluor 594 hydrazide	Invitrogen	Cat#: A10438
Calcium chloride dihydrate	Sigma	Cat#: 223506; CAS: 10035-04-8
D-(+)-Glucose	Sigma	Cat#: G7021; CAS: 50-99-7
Guanosine 5′-triphosphate sodium salt hydrate	Sigma	Cat#: G8877; CAS: 36051-31-7
HEPES	Sigma	Cat#: H3375; CAS: 7365-45-9
Isoflurane	Patterson Veterinary	Cat#: 07-893-1389
Magnesium chloride hexahydrate	Sigma	Cat#: 63068; CAS: 7791-18-6
Oregon Green 488 BAPTA-1, Hexapotassium Salt, cell impermeant	Invitrogen	Cat#: O6806
Phosphocreatine di(tris) salt	Sigma	Cat#: P1937; CAS: 108321-17-1
Potassium chloride	Sigma	Cat#: 60128; CAS: 7447-40-7
Potassium D-gluconate	Sigma	Cat#: G4500; CAS: 299-27-4
(+)-Sodium L-ascorbate	Sigma	Cat#: 11140; CAS: 134-03-2
Sodium bicarbonate	Sigma	Cat#: 792519; CAS: 144-55-8
Sodium chloride	Sigma	Cat#: S7653; CAS: 7647-14-5
Sodium phosphate monobasic monohydrate	Sigma	Cat#: S9638; CAS: 10049-21-5
Sodium pyruvate	Sigma	Cat#: P2256; CAS: 113-24-6
Sucrose	Sigma	Cat#: S1888; CAS: 57-50-1
Tetrodotoxin citrate	Abcam	Cat#: ab120055; CAS: 18660-81-6
Tetrodotoxin	Tocris	Cat#: 1078; CAS: 4368-28-9
Experimental Models: Organisms/Strains		
C57BL/6	Jackson laboratory	Stock No: 000664
RBP4-cre	MMRRC	Stock No: 037128-UCD
Software and Algorithms		
ImageJ	National Institutes of Health	https://imagej.nih.gov/ij/index.html
MATLAB 9.1	MathWorks	https://www.mathworks.com
Other		
Axopatch 200B	Axon Instruments	N/A
Dagan BVC-700A	Dagan corporation	N/A
Electro-optical modulator	Conoptics	M350-80
Leica VT1200 S Fully automated vibrating blade microtome	Leica	VT1200 S
Mai Tai DeepSee	Spectra-Physics	MAI TAI HP DS
InSight DeepSee	Spectra-Physics	InSight DS DUAL
Photosensor module	Hamamatsu	H7422A-40

REAGENT or RESOURCE	SOURCE	IDENTIFIER
Photosensor module	Hamamatsu	H7422P-40
Ultima In Vitro Multiphoton Microscope System	Bruker	N/A
Neurolabware standard microscope	Neurolabware	N/A
Fast electrically tunable-lens	Optotune	EL-10-30-NIR-LD

Author Manuscript Author Manuscript Author Manuscript Author Manuscript